Surface Engineering of Bioabsorbable Zinc Implants with new Antibiotic Coordination Frameworks

Juliana Mota[1*]
[1]Centro de Química Estrutural, Instituto Superior Técnico, Universidade de Lisboa, Av. Rovisco Pais, 1, 1049-001 Lisboa, Portugal;
[*]juliana.ferreira.mota@tecnico.ulisboa.pt

Abstract

Antibiotic coordination frameworks' design arose from the need to find more effective drugs to fight infectious diseases. Herein it has been proven that ACF1 is a viable compound to improve the antibacterial activity of already available antibiotics, through mechanochemistry synthetic routes. The design of ACF1 was successfully achieved with nalidixic acid (NALD), a quinolone antibiotic, that can coordinate with a variety of metals to form new structures with improved bioactivity. The herein described coordination of nalidixic acid with Ca(II), an important bone mineral, and the knowledge that infections easily occur during implantation prompted us to explore the use of such compounds as functional coatings on bone implantable materials. Salicylic acid was used as a second ligand to build a MOF structure.
The physicochemical analysis of the NALD-SA-Ca (ACF1), prior to and after Zn functionalization, confirmed that the stability of the newly synthesized drug was preserved. The influence of this functional coating on Zn, a bioresorbable metal aiming to assist bone-healing, was investigated and this new biomaterial degradation and biocompatibility were discussed.

Keywords: Active pharmaceutical ingredient, calcium, implant, mechanochemistry, nalidixic acid, zinc.

Introduction

Implantable devices have become a preferred treatment option for the rehabilitation of partially ruptured bone or bone tissues. These are conditions with an increasing incidence in our ageing society, where bone fractures arising from falls are incredibly high. In an era where antibiotic resistance is increasing, bacterial infections associated with implanted materials can lead to rejection, leading to implant removal or in severe cases, even death(1).

The success of the implanted materials can increase with the use of biocompatible and bioabsorbable implants, such as Zinc (Zn) (2, 3), shown as promising non-permanent implants, that will degrade while bone recovers over time, thus avoiding a second surgery for implant removal and associated infections.

To ensure the success of this strategy, local delivery of antibiotics upon implantation are state-of-the-art approaches to overcome the increasing threat of infections related to these medical interventions.

The inappropriate use of antibiotics has caused an undesired effect: the ability of bacteria to develop resistance mechanisms to these drugs, which nowadays represents a major global health problem. This threat has a direct impact on the development of infections associated with implantable devices, a medical intervention with increasing incidence in our ageing society.

Bearing in mind the need to find more efficient drugs, able to be used in local drug delivery systems, antibiotic coordination frameworks (ACFs) have been successfully explored through mechanochemistry, as a way to increase the antimicrobial activity and stability of the already commercially available antibiotics. This expedite strategy can result in a fast delivery of a novel antimicrobial solution, for which an easier acceptance by pharmaceutical regulators is expected.

In particular, the ability of nalidixic acid, a quinolone antibiotic, to coordinate to different metals, resulting in new forms with improved properties and activity has been proven (4-6). The specific coordination of nalidixic acid to Ca(II) centers, an important bone mineral, is of utmost relevance when envisaging bone-healing applications. The combination of nalidixic acid with Ca(II) in the design of a new AFC represents

a step forward as a combination of antibacterial properties and increased bone-healing stimulation can be achieved. The use of salicylic acid as a second ligand in the design of this system offers the potential for combined activities, as salicylic acid has anti-inflammatory and even antibacterial properties(7).

This work aimed at designing a new ACF by mechanochemistry techniques with bifunctional bioactivity. The local delivery of this new drug was achieved by the design of functional coatings on Zn. The impact on the degradation and biocompatibility of this bioresorbable material was assessed by electrochemical techniques.

Experimental Section

Reagents

All reagents and solvents were acquired from Sigma – Aldrich and used without modification; zinc was acquired from Goodfellow.

Synthesis of ACF1: Nalidixic acid, salicylic acid and calcium hydroxide, in a proportion of 3:1:2, were mechanically ground with 200 μL of water for 5 min in a Retsch MM400 ball mill operating at a frequency of 29 s^{-1}, using 15 mL stainless steel snap closure grinding jars, with 2 stainless steel balls (7 mm diameter). A dry powder, compound ***ACF1***, was obtained and analysed by XRPD and has shown to be a new product without any traces of the precursor reagents.
Single crystals of ***ACF1*** were obtained by recrystallization in methanol and ammonia, by slow evaporation of the solvents, at room temperature.

Coatings' formulation: The as-synthesized ACF1 was deposited on Zn by electrophoresis. For that purpose, a two-cell electrochemical system was used with Zn as the working electrode and Pt as the counter electrode. Prior to electrophoresis, Zn surface was polished with sandpaper with a grit of P600 (Gravimeta). The electrolyte used was water with ACF1 (5 mg/mL). The electrophoresis procedure was made with a Gamry instruments interface 1010E, by applying 10V for 1200 and 3600s.

Physicochemical characterization:
Both the ACF1 powder and coated Zn (prior and after immersion tests) were physicochemically analysed by X-ray powder diffraction (XRD) and scanning electron microscopy (SEM), with the chemical analysis being performed by the corresponding Energy-dispersive X-ray spectroscopy (EDS). A deeper structural analysis of ACF1 was attained by Single-Crystal X-Ray Diffraction (SCXRD); also, Differential Scanning Calorimetry (DSC) and Thermogravimetric Analysis (TGA) were performed.

Single-Crystal X-Ray Diffraction (SCXRD): Crystals of ACF1, ACF2 and ACF3 suitable for X-ray diffraction studies were mounted on a loop with Fomblin© protective oil. SCXRD data were collected on a Bruker AXS-KAPPA D8QUEST, at 293 K, with graphite-monochromated radiation (Mo Kα, λ=0.71073 Å). The X-ray generator was operated at 50 kV and 30 mA and the X-ray data collection was monitored by the APEX3 program. All data were corrected for Lorentzian polarization and absorption effects using SAINT(8) and SADABS(9) programs. SHELXT(10) was used for structure solution and SHELXL-97(10) was used for full-matrix least-squares refinement on F2. These two programs are included in the package of programs WINGX-Version 2014.1(11). A full-matrix least-squares refinement was used for the non-hydrogen atoms with anisotropic thermal parameters. H_{OH} atoms were added in calculated positions. H_{NH} atoms were located from different Fourier maps and refined. H_{CH} and HOH atoms were added in calculated positions and refined riding on their respective C and O atoms. MERCURY 2020.3.0(12) was used for packing diagrams. PLATON(13) was used for hydrogen bond interactions. Crystallographic details are given at **Table 1**.

Table 1. Crystallographic details for ACF1.

	ACF1
Chemical formula	$C_{43}H_{37}N_6O_{20}Ca_2$
M_r	1037.95
T / K	298
Morphology, colour	Block, colourless
Crystal size / mm	0.32x0.16x0.02
Crystal system	Triclinic
Space group	*P*-1
a / Å	12.2952(16)
b / Å	12.6162(15)
c / Å	16.2844(18)
α / °	77.517(3)
β / °	85.482(3)
γ / °	84.262(3)
V / Å³	2449.7(5)
Z	2
d / mg.m⁻³	1.407
μ / mm⁻¹	0.316
θ min / °	2.250
θ max / °	26.473
Reflections collected/unique	33419/9669
R_{int}	0.1568
GoF	1.001
R_1 *(obsd), ans wR2 (> 2σ(I))*	0.0932, 0.2320

Powder X-Ray Diffraction (PXRD): data were obtained in a D8 Advance Bruker AXS θ–2θ diffractometer (Bruker, Karlsruhe, Germany) equipped with a LYNXEYE-XE detector, using a copper radiation source (Cu Kα, λ = 1.5406 Å), operated at 40 kV and 30 mA. Data was collected in the 3–60° 2θ range a step size of 0.02°, and 0.6 s per step. The program MERCURY 2020.3.0 (12) was used for the calculation of X-ray powder patterns on the basis of the single-crystal structure determinations.

Differential Scanning Calorimetry (DSC) and Thermogravimetric Analysis (TGA): Combined TG-DSC measurements were carried out on a SETARAM TG-DTA 92 thermobalance under nitrogen flow with a heating rate of 10 ºC.min-1. The samples weights were in the range of 5-10 mg.

Scanning electron microscopy (SEM): The images were acquired either in JEOL-JSM7001 F or Hitachi S2400 apparatus and the elemental chemical composition was evaluated by the corresponding X-ray energy dispersive spectrometer (EDS). Whenever required, the samples' conductivity was increased by applying a layer of conductive gold/palladium with a Polaron E-5100.

Electrochemical impedance spectroscopy (EIS): To assess the *in vitro* degradation of the Zn coated with ACF1, electrochemical impedance spectroscopy (EIS) measurements were performed. For this test, samples were immersed in simulated body fluid (SBF) solution [NaCl 137.5 mM, $NaHCO_3$ 4.2 mM, KCl 3.0 mM, K_2HPO_4 1.0 mM, $MgCl_2 \cdot 1.5$ mM, $CaCl_2$ 2.6 mM, Na_2SO_4 0.5 mM, $(HOCH_2)_3CNH_2$ 50.5 mM at pH 7.4] at 37 °C (14). EIS measurements were carried out in a three-electrode electrochemical cell with the functionalized samples as WE, platinum coil as counter electrode and SCE as reference. These measurements were carried out in a Gamry 600+ by applying a 10 mV rms perturbation within a frequency range from 10^5 Hz down to 10^{-2} Hz. EIS spectra were periodically recorded at open circuit potential (OCP). The resulting EIS data was plotted with the Zview software.

Results and Discussion

A new compound was obtained by mechanochemically reacting nalidixic acid, salicylic acid and calcium hydroxide (**Fig. 1**).

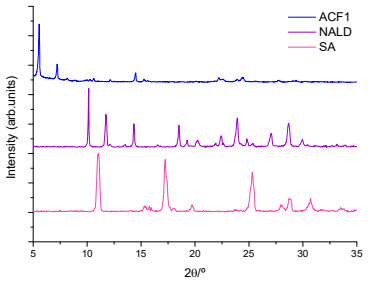

a)

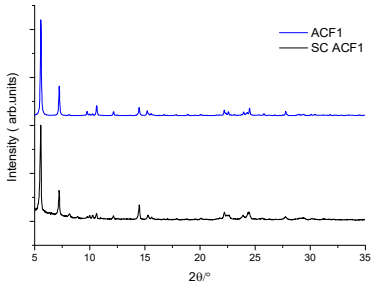

b)

Figure 1. PDRX patterns for a) ACF1 (blue), nalidixic acid (purple), and salicylic acid (pink); b) ACF1 (blue) and pattern from simulated the crystal structure (black)

The results of the PXRD indicate, by comparison of the starting reagents' and experimental pattern (**Fig. 1a**), that the reaction yielded pure ACF1, with the final bulk product having no traces of any of the starting materials. From a comparison between the simulated diffraction pattern and experimental powder pattern (**Fig. 1b**) confirmed the purity of the bulk.

The SCXRD analysis showed that the asymmetric unit of ACF1 consists of two crystallographically independent Ca(II) metal centers, three nalidixic acids, one salicylic acid, three coordinated water molecules and five hydration water molecules (**Fig. 2a**). The crystal structure confirms the coordination of nalidixic acid to the Ca(II) centers by the carboxylate and carbonyl moieties, while salicylic acid coordinates only by the carboxylate moiety. One of the Ca sites coordinates to the three nalidixic acid anions and assumes a square antiprismatic geometry (CN=8), while the other Ca center coordinates to both nalidixic and salicylic acids anions and water molecules displaying an octahedral geometry (CN=6) (**Fig. 2b**). Moreover, the supramolecular arrangement of ACF1 is characterized by the formation of 1D frameworks, in a view along the *b* axis, where the hydration water molecules occupy the space between consecutive 1D frameworks (**Fig. 2c**).

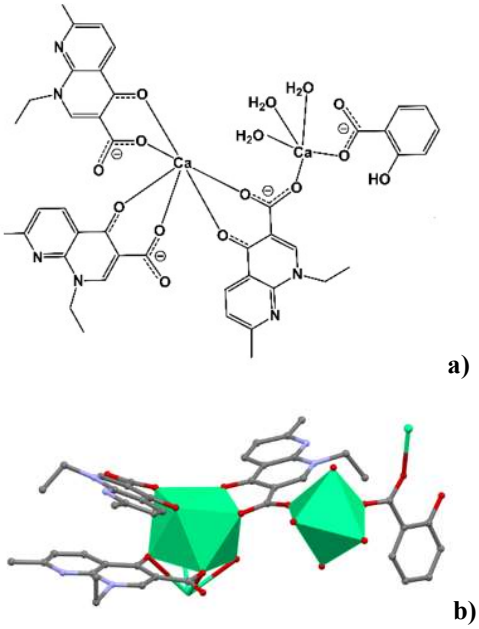

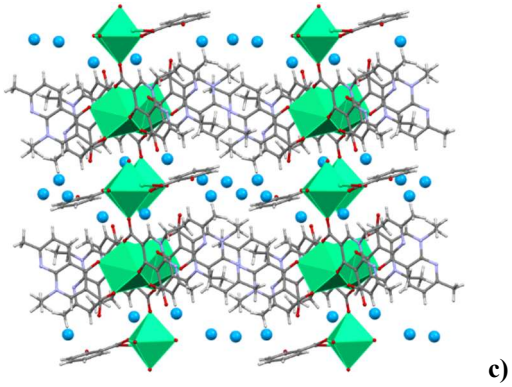

Figure 2. Details on ACF1 crystal structure depicting the: a) details of the coordination to the Ca(II) metal centers; b) coordination Ca(II) geometries. Hydrogen atoms were omitted for clarity; c) Crystal Packing of ACF1. Hydration water molecules are represented in blue, using space fill style, for clarity

The morphological analysis revealed that the powder possesses a laminae appearance with length variations between 0.3 to 0.6 µm, with a superior dominance over the minimum length of 0.3 µm (**Fig 3a**) where an even distribution of Ca was observed (**Fig 3b**).

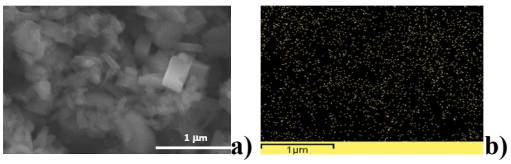

Figure 3. a) Morphological structure of ACF1; b) Atomic distribution of Calcium on ACF1

Aiming the commercialization of this new compound, its stability was assessed after 6 months of storage (**Fig.5**) and by DSC, as well as by TGA (**Fig. 4**).

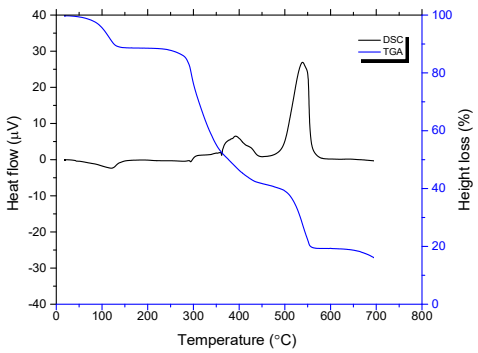

Figure 4. DSC and TGA of ACF1

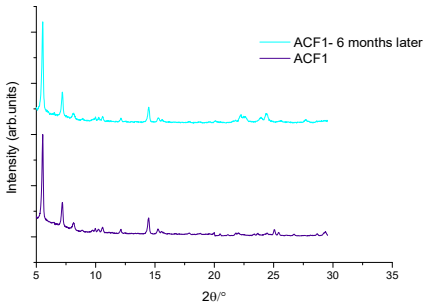

Figure 5. Stability analysis of ACF1

ACF1 kept its structure after 6 months (**Fig.5**) and was stable until approximately 100ºC, the temperature at which the loss water present in its structure is detected, corresponding to 11.2% weight loss (theoretical 13.6%) until 120.4°C. After 250°C several decomposition phenomena are detected (**Fig. 4**).

These results lead to the formulation of a new coating on Zn aiming at the local delivery of this ACF as a novel antimicrobial able to further support bone-healing activity.

For this purpose, two coatings were designed by electrophoretic techniques (**Fig. 6**), by depositing ACF1 for 1200s (ZnACF1-1) and 3600s (ZnACF1-2) on Zn surface.

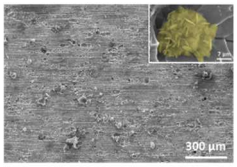

a)

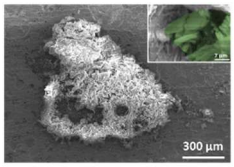

b)

Element	% Atomic SP ZnACF1-1	% Atomic SP ZnACF1-2
Carbon	78.0	78.0
Zinc	12.2	16.7
Oxygen	8.1	3.6
Calcium	1.7	1.7

Figure 6. Morphological analysis of the ACF1 coatings; SEM images of the Zn surface with ACF1 deposited a) ZnACF1-1 and b) ZnACF1-2; insets show in detail deposits of ACF1 on Zn and their elemental composition for both depositions.

This seldom attempt approach resulted in two distinct coatings of ACF1 (**Fig. 6**), confirmed by PXRD analysis (data not shown), where the diffraction pattern was preserved after the deposition and EDS, in which the expected C, O and Ca were detected. In both cases, islands of ACF1 deposited were visible on the surface, as well as several holes caused by Zn degradation, showing the ACF1 deposition was made at the expense of Zn dissolution. The main difference between the two coatings is related to the holes, while in ZnACF1-1 there are several and well-defined holes, in ZnACF1-2 the degradation was so extensive that a rough surface (instead of holes) was developed along with the deposition. In both cases, as referred, islands of ACF1 were depicted and additionally in ZnACF1-2 big extensions of ACF1 deposits were also visible on the surface. Interestingly the lamina-like structures of the ACF1 deposits were slightly different, whereas the laminas formed on ZnACF1-1 were smaller when compared with ZnACF1-2, these were larger (insets in **Fig. 6**).

To understand the impact that this functionalization had on Zn degradation EIS analyses were performed (**Fig. 7**). The Nyquist plots showed that both bare Zn and ZnACF1-1 have similar behaviors, with the semi-circles suggesting similar corrosion resistance behaviors; a small slop tending to 45º suggests that active corrosion may be occurring through pitting. The plot for the ZnACF1-2, with a large semi-circle, indicates a higher corrosion resistance, when compared with bare Zn or ZnACF1-1 (**Fig. 7a**).

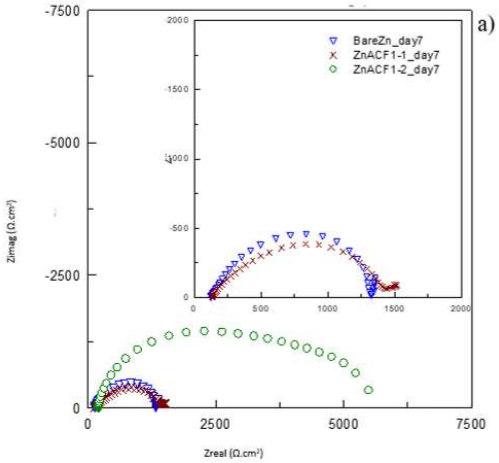

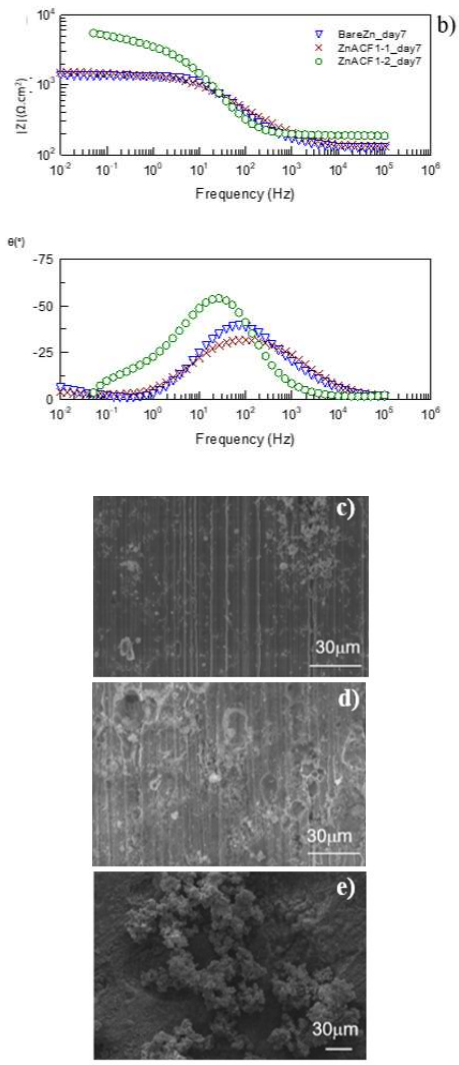

Figure 7. Degradation behavior of ACF1 coated Zn samples; a) Nyquist, b) Bode plots and SEM images of c) bare Zn, d) ZnACF1-1 and e) ZnACF1-2 after 7 days of immersion in SBF at 37 ºC.

The value of |Z| at lower frequencies shows that ZnACF1-2 has the highest corrosion resistance, whereas both bare Zn and ZnACF1-1 have similar corrosion resistances. These results suggest that despite the holes formed on ZnACF1-2, the corrosion onset resulted in a more protective surface than in the case of both bare zinc and ZnACF1-1 (**Fig. 7b**). This means that upon corroding, the protective effect of the ACF1-2 coating super passed the detrimental effect of the hole formed on the sample surface. When comparing the phase angle plots, there is clear evidence that the time constant appearing in the middle frequency range, referring to the resulting corrosion products formed upon immersion, are quite distinct. Both in bare zinc and ZnACF1-1, despite the similar protectiveness, the nature of the resulting products is different. The most protective corrosion products, achieved on ZnACF1-2 sample, is visible by the highest phase angle in the middle frequency range (**Fig. 7b**).

The corrosion products reported in the bibliography are presented in Table 2(15-17):

Table 2. Chemical composition of corrosion products

Corrosion product	Chemical composition
Zincite	ZnO
Zinc hydroxide	$Zn(OH)_2$
Hydrozincite	$Zn_5(OH)_6(CO_3)_2$
Hopeite	$Zn_3(PO4)_2$
Smithsonite	$ZnCO_3$
Skorpionite	$Ca_3Zn_2(PO_4)_2CO_3(OH)_2$
Simonkolleite	$Zn_5(OH)_8Cl_2$
Hydroxyapatite	$Ca_5(PO_4)_3(OH)$

Morphologically the surfaces of the substrates are completely different: Zn, without any coating, was the sample with the least amount of corrosion products; on the coated samples different morphologies were revealed. Their elementary compositions are shown in **Table 3.**

Table 3. Elemental composition of the corrosion products for samples Zn, ZnACF1-1 and ZnACF1-2

% At. SP	ZnBare_day7	ZnACF1-1_day7	ZnACF1-2_day7
O	12.7	25.9	49.7
C	24.4	14.2	16.56
Ca	1.0	3.4	3.8
Zn	59.0	48.3	23.0
P	2.9	7.4	5.3
Cl	n.d.	0.8	1.8

Upon an overall comparison of the corrosion layer formed on ZnACF1-1 and ZnACF1-2, there is a notable increase in Ca content in ZnACF1-2. This, expected to form hydroxyapatite can endow ZnACF1-2 with increased biocompatibility.

In an attempt to identify this important inorganic compound, the corroded substrates were analyzed by XRD. For sample ZnACF1-1 no signs of crystalline corrosion products were

recorded. Whatsoever, a peak was successfully obtained for the corroded ZnACF1-2 sample for a 2θ value of approximately 11°, a peak that is regularly identified in the literature for the presence of hydroxyapatite (18-20).

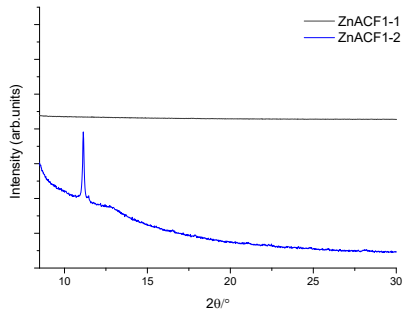

Figure 8: PRXD pattern of substrate after immersion for sample ZnACF1-1 (black) and ZnACF1-2 (blue)

The high Ca content and XRD analysis (**Fig.11**) are strong indications for the formation of hydroxyapatite, a compound that has a major interest in this study, as it is shown to be important on the success of bone implants. By improving the cytocompatibility towards human bone cells, hydroxyapatite is responsible to promote osteoconductive and biosorption properties. The increased capability of reabsorption of molecules responsible for the recovery of bone may therefore improve the desirable properties of the biomaterial presented herein.

Conclusions

ACF1 was successfully synthesized by mechanochemistry, and has shown to be a new antibacterial agent, with potential for bone-healing applications. ACF1 corresponds to a stable 1D framework, with Ca(II) sites assuming square antiprismatic (CN=8) and octahedral (CN=6) geometries. The antibacterial activity of the new ACF against *E. coli* and *S. aureus* was preserved when compared with its precursors. Zn, a well-accepted bioresorbable material used for bone implant applications, was successfully functionalized with ACF1 by electrophoresis. The designed coatings were built up at the expense of Zn dissolution. The combinations of island ACF1 deposition and Zn dissolution morphology rendered a higher corrosion resistance and biocompatibility to ZnACF1-2, the electrodeposition procedure using a superior deposition time.

The results attained herein proved the potential to combine and improve the antimicrobial and healing capability of surface functionalization with newly designed antibiotics. There is still a long way to go, as Zn dissolution is a drawback in this procedure. Also, release studies are required to understand the feasibility of the bioactivity of these new biomaterials.

Acknowledgements:

Authors acknowledge funding to Fundação para a Ciência e a Tecnologia (projects UIDB/00100/2020, UIDP/00100/2020 and PTDC/QUI-OUT/30988/2017, and contracts under DL No. 57/2016 regulation, and CEECIND/00283/2018) and FEDER, Portugal2020 and Lisboa2020 (project LISBOA-01-0145-FEDER-030988).

Dr. Vânia André, Dr. Marta M. Alves, Prof. M. Fátima Montemor.

Dr.Auguste Fernandes is acknowledged for TGA and DSC data.

Notes and References

Crystallographic information files (CIF) are accessible for the crystal structure; it has also been deposited at the Cambridge Crystallographic Data Centre (CCDC).

References

1. Rahim M.I., Ullah S., Mueller P.P. Advances and Challenges of Biodegradable Implant Materials with a Focus on Magnesium-Alloys and Bacterial Infections. Metals. 2018;8(7).
2. Alves M.M., Marques L.M., Nogueira I., Santos C.F., Salazar S.B., Eugenio S., In silico, in vitro and antifungal activity of the surface layers formed on zinc during this biomaterial degradation. Applied Surface Science. 2018;447:401-7.
3. Yang H.T., Wang C., Liu C.Q., Chen H.W., Wu Y.F., Han J.T., Evolution of the degradation mechanism of pure zinc stent in the one-year study of rabbit abdominal aorta model. Biomaterials. 2017;145:92-105.
4. Bravo C., Galego F., Andre V. Hydrogen bonding networks of nalidixic acid-copper(II) complexes. Crystengcomm. 2019;21(47):7199-203.
5. André V., Galego F., Martins M. Mechanochemical Assembly of Nalidixic Acid Bioinspired Metal-Organic Compounds and Complexes toward Improved Solubility. Crystal Growth & Design. 2018;18(4):2067-81.
6. André V., da Silva A.R.F., Fernandes A., Frade R., Garcia C., Rijo P., Mg- and Mn-MOFs Boost the Antibiotic Activity of Nalidixic Acid. Acs Applied Bio Materials. 2019;2(6):2347-54.
7. Salicylic acid 2021. *PubChem*.[https://www.ncbi.nlm.nih.gov/pubmed/.] (last acessed 14 July 2021)
8. Bruker AXS: SAINT+, release 6.22. Bruker Analytical Systems: Madison,WI. 2005.
9. Bruker AXS:SADABS. Bruker Analytical Systems: Madison,WI. 2005.
10. Sheldrick GM. A short history of SHELX. Acta Crystallographica Section A. 2008;64:112-22.
11. Farrugia LJ. WinGX - Version 1.80.05. J Appl Cryst. 1999;32:837-8.
12. Macrae C.F., Bruno I.J., Chisholm J.A., Edgington P.R., McCabe P., Pidcock E., Mercury CSD 2.0 - new features for the visualization and investigation of crystal structures. Journal of Applied Crystallography. 2008;41:466-70.
13. Spek A.L. Single-crystal structure validation with the program PLATON. Journal of Applied Crystallography. 2003;36:7-13.
14. Kokubo T., Takadama H. How useful is SBF in predicting in vivo bone bioactivity? Biomaterials. 2006;27(15):2907-15.
15. Alves M.M., Mil-Homens D., Pinto S., Santos C.F., Montemor M.F. Antagonist biocompatibilities of Zn-based materials functionalized with physiological active metal oxides. Colloids and Surfaces B-Biointerfaces. 2020;191.
16. Alves M.M., Prošek T., Santos C.F., Montemor M.F. Evolution of the in vitro degradation of Zn–Mg alloys under simulated physiological conditions. 2017.
17. Alves M.M., Cunha D.V., Santos C.F., Mira N.P., Montemor M.F. In vitro corrosion behaviour and anti-Candida spp. activity of Zn coated with ZnO-nanostructured 'Anastacia' flowers. Journal of Materials Chemistry B. 2016;4(27):4754-61.
18. Jayabalan M., Shalumon K.T., Mitha M.K., Ganesan K., Epple M. The effect of radiation processing and filler morphology on the biomechanical stability of a thermoset polyester composite. Biomedical Materials. 2010;5(2).
19. Manafi S.A., Yazdani B., Rahimiopour M.R., Sadrnezhaad S.K., Amin M.H., Razavi M. Synthesis of nano-hydroxyapatite under a sonochemical/hydrothermal condition. Biomedical Materials. 2008;3(2).
20. Calasans-Maia M.D., de Melo B.R., Alves A., Resende R.F.D., Louro R.S., Sartoretto S.C., Cytocompatibility and biocompatibility of nanostructured carbonated hydroxyapatite spheres for bone repair. Journal of Applied Oral Science. 2015;23(6):599-608.